Baryon stopping and partonic plasma production by strong chromofields

K. A. Lyakhov and H. J. Lee
Department of Nuclear and Energy Engineering, Jeju National University, Ara-dong 1, Jeju 690-756, South Korea

I. N. Mishustin
Frankfurt Institute for Advanced Studies, J.W. Göthe Universität, Ruth-Moufang-Strasse 1, D-60438 Frankfurt am Main, Germany
The Kurchatov Institute, Russian Research Centre, Kurchatov Square 1, 123182 Moscow, Russia
(Received 31 January 2011; revised manuscript received 3 August 2011; published 2 November 2011)

Strong chromofields developed at early stages of relativistic heavy-ion collisions give rise to the collective deceleration of net baryons from colliding nuclei. We have solved classical equations of motion for baryonic slabs under the action of a time-dependent chromofield. We have studied the sensitivity of the slab trajectories and their final rapidities to the initial strength and decay pattern of the chromofield as well as to the back-reaction of produced plasma. This mechanism can naturally explain significant baryon stopping observed at Relativistic Heavy Ion Collider corresponding to an average rapidity loss $\langle \delta y \rangle \approx 2$. Using a Bjorken-like hydrodynamical model with a particle production source term, we also study the evolution of partonic plasma produced as the result of chromofield decay. Due to the delayed formation and expansion of plasma, its maximum energy density is much lower than the initial energy density of the chromofield. Predictions of baryon stopping for Pb + Pb collisions at Large Hadron Collider energies were made.

DOI: 10.1103/PhysRevC.84.055202 PACS number(s): 12.38.Mh, 25.75.Nq, 25.75.Dw

I. INTRODUCTION

It is expected that strong color fields are generated at early stages of ultrarelativistic heavy-ion collisions. There exist various suggestions concerning the space-time structure of these fields from stringlike configurations as in the color flux-tube model [1] to more complicated configurations of the Weizsäcker-Williams type [2]. This picture is most conveniently presented in the c.m. frame where two Lorentz contracted nuclei look like thin sheets. After the intersection these sheets acquire stochastic color charges as a result of multiple soft gluon exchange. This leads to the formation of strong longitudinal color fields in the space between the receding sheets. A qualitative view of the nuclear sheets and generated chromofields is presented in Fig. 1. At later stages, the fields decay into quarks and gluons, which after equilibration form a quark-gluon plasma. This process has been studied by several authors under different assumptions about the field decay mechanism (see, e.g., Refs. [3–6]).

Most calculations assume that after collision the nuclei follow light-cone trajectories, thus disregarding their energy losses for producing the chromofield. For instance, such an assumption was made in the McLerran-Venugopalan (MV) model [6,7], assuming that color sources are moving along the light cone and produce classical Yang-Mills radiation (see also Ref. [8]). Similar assumption was made also in Ref. [9], where classical Yang-Mills equations were solved within the color flux-tube model (FTM).

Such a recoilless approximation is irrelevant for studying the baryon stopping. Obviously, the energy of produced particles and fields is taken entirely from the kinetic energy of colliding nuclei. As measured by the BRAHMS collaboration [10], in central Au + Au collisions at highest Relativistic Heavy Ion Collider (RHIC) energy $\sqrt{s_{NN}} = 200$ GeV the nuclear energy loss is very large, about 70% of the initial kinetic energy. The peaks in the net-baryon rapidity distribution are substantially shifted toward the center of mass from the initial rapidities $\pm y_0$. The average net-baryon rapidity loss is estimated to be $\langle \delta y \rangle \approx 2.0$.

The problem of baryon stopping at RHIC has been addressed recently by several authors. In particular, net-baryon rapidity distributions were calculated within the microscopic string-based models like Ultrarelativistic Quantum Molecular Dynamics (UrQMD) [11] and Quark Gluon String Model (QGSM) [12]. Although these models implement energy and momentum conservation and thus predict a certain baryon stopping, they are formulated in momentum space and cannot give a space-time picture of this process. Also, they are dealing with hadronic secondaries and therefore preclude the quark-gluon plasma formation. The distribution of valence quarks at midrapidities was also studied in Ref. [13] within a QCD-motivated approach which, however, cannot be applied for the fragmentation regions. Over a decade ago the Parton cascade model (PCM) was developed based on parametrization of the nucleonic parton distribution function to describe the baryon rapidity distributions [14]. Moreover, successful parametrization of the nuclear parton distribution function can be also sufficient to reproduce net-baryon rapidity density. Such parametrizations were proposed in [15]. From the website of Ref. [16] the Fortran subroutine generating parton distribution functions for most nuclei in Mendeleev's table can also be downloaded.

In Ref. [17] a simple space-time model was proposed, where baryon stopping was directly linked to the formation of strong chromofields. The nuclear trajectories were calculated there under the assumption that the field is neutralized at some sharp proper time $\tau = \sqrt{t^2 - z^2} = const$. In this paper we improve this model for the general case when both the time-dependent chromofield and partonic plasma are present. It is remarkable

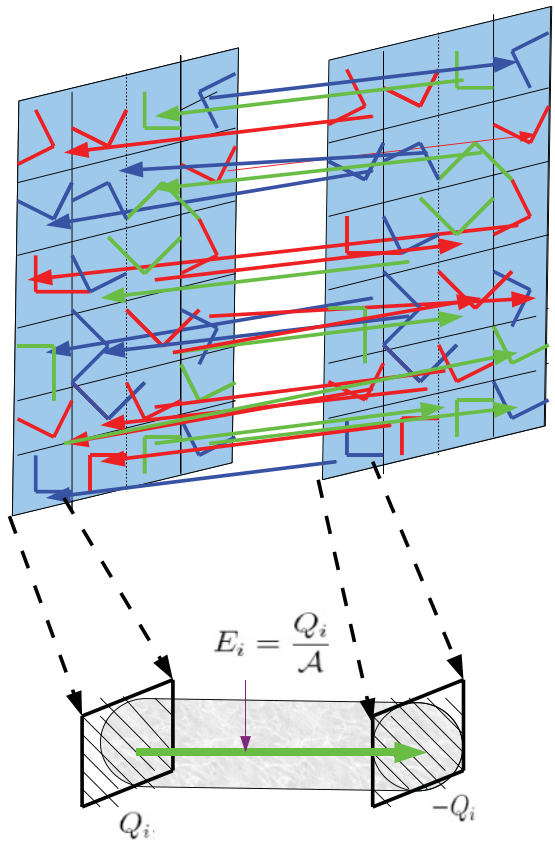

FIG. 1. (Color online) Longitudinal and transverse components of MV chromofield produced by stochastic color charges generated on nuclear sheets after collision, as proposed in Ref. [2]. Directions of the field can be opposite, but total force between the slabs is attractive. Each slab area is subdivided on smaller elements or spots of minimal area $s_\perp = \pi a^2 = \frac{\pi}{Q_i^2}$, which can be resolved by a hard probe of given energy. The classical field produced between two spots with opposite charges Q_i has a color flux-tube configuration displayed on the bottom figure.

that the nuclear trajectories can be expressed in a simple analytical form for an arbitrary time dependence of the chromofield. The basic idea is the same as in Ref. [17], i.e., to derive equations of motion of the baryonic slabs from the energy and momentum conservation laws. This approach makes it possible to relate the degree of baryon stopping and the energy density of partonic plasma to the strength of the chromofield generated at the initial stage of the reaction. A short presentation of our results was given previously in Ref. [18].

II. BARYONIC SLABS

We consider only beam energies so high that before collision the nuclei can be thought of as very thin, Lorentz-contracted sheets. Each sheet is divided into many small elements or slabs of transverse area σ_0 labeled by an index a where $a = p$ for the projectile nucleus and $a = t$ for the target nucleus (see Fig. 1). Each slab is characterized by a baryon number N_a, which is assumed to be strictly conserved.

We decompose a nucleus-nucleus collision into a multitude of pairwise collisions of individual slabs from projectile and target nuclei. Moreover, we assume that before and after the overlap at $t = 0$, both slabs propagate as rigid bodies in opposite directions along the beam axes z. The energy and momentum of slab a per unit area is parametrized in terms of its mass M_a and longitudinal rapidity Y_a (for more details see Ref. [19]):

$$E_a = M_a \cosh Y_a,\ P_a = M_a \sinh Y_a. \tag{1}$$

It is convenient to express M_a as

$$M_a = m_\perp \tilde{N}_a, \tag{2}$$

where $m_\perp = \sqrt{m_N^2 + \langle p_\perp \rangle^2}$ is the baryon mean transverse mass, which is written in terms of the mean transverse momentum $\langle p_\perp \rangle$. As it is demonstrated later, the time evolution of $\langle p_\perp \rangle_\tau$ strongly depends on the interaction with partonic plasma.

In the Glauber model [20] the average number of participants at impact parameter $\mathbf{b}$ is determined by integration over a transverse plane:

$$N_{\rm part}(\mathbf{b}) = \int d^2\mathbf{s}[\tilde{N}_p(\mathbf{b},\mathbf{s}) + \tilde{N}_t(\mathbf{b},\mathbf{s})], \tag{3}$$

where

$$\tilde{N}_a(\mathbf{b},\mathbf{s}) = A_a T_a(\mathbf{b},\mathbf{s})\{1 - [1 - \sigma_{NN} T_{\bar{a}}(\mathbf{b},\mathbf{s})]^{A_{\bar{a}}}\} \tag{4}$$

is the number of participants from the nucleus a at transverse coordinate $\mathbf{s}$. Here A_a and $A_{\bar{a}}$ are baryon numbers of colliding nuclei, $\bar{a} = p$ for $a = t$ and vice versa, and σ_{NN} is the total inelastic NN cross section. The profile function $T_a(\mathbf{b},\mathbf{s})$ is introduced by integration of the baryon number density along the beam axis:

$$T_a(\mathbf{b},\mathbf{s}) = \frac{1}{A_a}\int \rho_a(\mathbf{r}) dz. \tag{5}$$

Below we use for $\rho_a(\mathbf{r})$ a Woods-Saxon parametrization consistent with nuclear data. It is obvious that the slab baryon number is given by

$$N_a(\mathbf{b},\mathbf{s}) = \sigma_0 \tilde{N}_a(\mathbf{b},\mathbf{s}). \tag{6}$$

The number of nucleon-nucleon collisions within the slab area σ_0 is

$$N_{\rm coll}(\mathbf{b},\mathbf{s}) = \sigma_0 \sigma_{NN} A_p A_t T_p(\mathbf{b}-\mathbf{s}) T_t(\mathbf{s}). \tag{7}$$

The value of σ_0 serves as the coarse-graining scale for sampling stringlike configurations stretched between the slabs. Final results are not very sensitive to the choice of σ_0, and below we take it equal to the inelastic NN cross section σ_{NN}.

III. REGION BETWEEN THE SLABS

At sufficiently high collision energies the slabs will go through each other, leaving behind a very unusual region occupied by strong chromofields and newly produced partons. It is most likely that vacuum condensates will be destroyed in this region so that chromofields and partons will live in a background of the perturbative QCD vacuum. We call this region a "QCD vacuum bubble" or simply, a "bubble." With time the bubble will expand, predominantly in the longitudinal direction, following the receding nuclear sheets. It is natural to

assume that chromofields and partons can exist only inside the bubble. By expanding the bubble the color charges, localized on baryonic slabs, do work against the physical vacuum at the expense of their kinetic energy. This picture follows from the Color Glass Condensate (CGC) initial state proposed in Ref. [2] and studied in numerous subsequent works. In general, both transverse and longitudinal fields can exist in bubble [6]. As shown in Ref. [21] by a numerical solution of the classical Yang-Mills equation, longitudinal chromoelectric and chromomagnetic fields practically of the same magnitude appear on the very early stage of reaction. The transverse components of the chromofield, which certainly appear in the Weizsäcker-Williams picture [2], in average will also act for the deceleration of color charges, but we shall put aside this issue until more detailed consideration. From a somewhat different point of view, the field configurations between the slabs can be represented as a collection of strings stretched between the projectile and target slabs. If the density of strings per unit transverse area is n and string tensions for each string are equal to $\sigma_i = \sigma$, then the energy density associated with this stringy field configuration is

$$\epsilon_f = \tfrac{1}{2}(\mathbf{E}+\mathbf{B})^2 = n\sigma. \tag{8}$$

In ultrarelativistic heavy-ion collisions the string density may be so high that the individual string picture becomes meaningless. As pointed out by several authors [22,23], at sufficiently high n the strings will fuse or even form percolated clusters, leading to more complicated configurations (see below). The energy-momentum tensor inside the bubble can be generally represented as

$$T^{\mu\nu} = T^{\mu\nu}_{\rm vac} + T^{\mu\nu}_{\rm field} + T^{\mu\nu}_{\rm part}, \tag{9}$$

where the terms in the right-hand side (rhs) correspond to the vacuum, chromofield, and partonic contributions, respectively. In the simplest consideration the vacuum contribution can be written as

$$T^{\mu\nu}_{\rm vac} = Bg^{\mu\nu}, \tag{10}$$

where B is the "bag constant." In a particular case when only the longitudinal chromofield is present, the energy-momentum tensor has the form

$$T^{\mu\nu}_{\rm field} = \epsilon_f {\rm diag}(1,1,-1,-1), \tag{11}$$

where ϵ_f is the energy density of the field. As explained in Ref. [24], by performing a proper Lorentz boost, one can obtain this diagonal form for the energy-momentum tensor for any field configuration, except the case when $\mathbf{E}$ and $\mathbf{B}$ are perpendicular and have equal values. By inspecting Eqs. (10) and (11) one can notice that the vacuum contribution corresponds to a positive energy density $\epsilon_{\rm vac} = B$ and a negative isotropic pressure $p_{\rm vac} = -B$, but the pressure associated with the chromofield is anisotropic, i.e., negative in the longitudinal direction and positive in the transverse direction with respect to the field. Therefore, particularly when $\epsilon_f = B$ the transverse pressure vanishes. This observation was used by several authors (see, e.g., Refs. [5,25–27]) for modeling the color flux tube by combining chromo-electro-magnetic and scalar fields. At the same time, the longitudinal pressure components for both the vacuum and the chromofield are both negative and act against of expansion of the bubble. In our calculations below we disregard effects of the transverse pressure on the slabs' longitudinal motion.

The last term in Eq. (9) is associated with the partonic contribution. This could be minijets produced at the very early stage of the collision [4], or partons produced later at the decay of the chromofield. We parametrize this contribution in a general form appropriate for a perfect fluid,

$$T^{\mu\nu}_{\rm part} = (\epsilon + p)u^\mu u^\nu - pg^{\mu\nu}, \tag{12}$$

where ϵ and p are the energy density and pressure of partonic plasma, and u^μ is its collective four-velocity. Different physical situations can be modeled by choosing different equations of state $p(\epsilon)$, ranging from a free-streaming partonic system ($p = 0$) to an ideal Quark-Gluon Plasma (QGP) ($p \approx \epsilon/3$). For our numerical simulations further on we will use only an ideal gas equation of state. Again, we assume that at early stages the plasma only expands in the longitudinal direction, i.e., $u^\mu = \gamma(1,0,0,v)$ and $\gamma = 1/\sqrt{1-v^2}$.

IV. INITIAL CHROMOFIELD ENERGY DENSITY

In this section we follow the ideas formulated in Refs. [2,6] and widely referred to now as the color glass condensate initial state. Within this picture random color charges are generated on the nuclear sheets as a result of soft gluon exchange at the interpenetration stage of a nuclear collision. In a single event these charges fluctuate from point to point in the transverse plane. The charges also fluctuate from event to event, so that in average over many events the areal charge is zero. It is convenient to introduce the color charge density $\rho(\eta, \mathbf{b}, \mathbf{s})$ as a function of coordinate in the transverse plane: $(\mathbf{b}, \mathbf{s})$ and longitudinal pseudorapidity, $\eta = \frac{1}{2}\ln\frac{t+z}{t-z}$. Following Refs. [2,6] we assume it as a stochastic variable distributed with the Gaussian weight:

$$P[\rho] \sim \exp\left[-\int d\eta d^2\mathbf{s}\frac{1}{2\mu_a^2(\eta,\mathbf{b},\mathbf{s})}Tr\rho^2(\eta,\mathbf{b},\mathbf{s})\right], \tag{13}$$

where μ_a^2 is the corresponding variance. For our estimates below we disregard possible dependence of μ_a on (**b,s**) and η. Then, after integrating out η in Eq. (13) we introduce a new color charge density as a function of only transverse coordinates,

$$\rho(\mathbf{b},\mathbf{s}) = \int d\eta\rho(\eta,\mathbf{b},\mathbf{s}), \tag{14}$$

which is treated as a random variable with the Gaussian weight

$$P[\rho] \sim \exp\left(-\frac{1}{2\mu_a^2}\int d^2\mathbf{s}Tr\rho^2(\mathbf{b},\mathbf{s})\right), \tag{15}$$

where Tr is taken over color indices.

These fluctuations are characterized by a certain scale in the transverse plane, which is related to the saturation scale $\mathcal{A} \approx \frac{1}{Q_s}$ introduced in high-density QCD [28]. Since the transverse size of the baryonic slabs σ_0 is assumed to be much larger, this means that many stringlike configurations (flux tubes) are stretched between the receding slabs. In this situation we can divide each slab into n small elements with equal transverse

area $\mathcal{A} = \frac{\pi}{Q_s^2}$, corresponding to the resolution scale $\sim \frac{1}{Q_s}$ of the hard probe at given energy, so that they cover the total slab area, i.e., $\sigma_0 = n\mathcal{A}$. Each flux-tube configuration connects the spots of opposite charge $\pm Q_i$ as in a capacitor. In the Abelian approximation the chromofield strength in a static flux tube is obtained from the Gauss theorem [5],

$$E_i = \frac{Q_i}{\mathcal{A}} \equiv \rho_i. \tag{16}$$

Then the force acting between opposite spots or string tension σ_i is

$$F_i = \tfrac{1}{2} Q_i E_i = \tfrac{1}{2}\rho_i^2 \mathcal{A} = \mathcal{A}\epsilon_i = \sigma_i, \tag{17}$$

where ϵ_i is the energy density of the chromofield in the color flux tube. For simplicity we neglect contribution of the bag constant here. It is important to note that all flux tubes produce attractive force between opposite spots on the projectile and target slabs. The force lines and their structure are schematically displayed in Fig. 1. The total force acting on each slab is then

$$F_a = \sum_{i=1}^{n} F_i = \frac{1}{2}\mathcal{A}\sum_{i=1}^{n}\rho_i^2, a = p, t. \tag{18}$$

Accordingly, we can represent the integral in Eq. (15) as the sum over all elements, so that

$$P(\rho_1, \ldots, \rho_n) \sim \exp\left(-\frac{\mathcal{A}}{2}\sum_{i=1}^{n}\frac{\rho_i^2}{\mu_i^2}\right) = \prod_{i=1}^{n}\exp\left(-\frac{\mathcal{A}\rho_i^2}{2\mu_i^2}\right). \tag{19}$$

Obviously, the event-by-event distribution of color charge in each element follows the Gaussian distribution:

$$P(\rho_i) = \sqrt{\frac{\mathcal{A}}{2\pi\mu_i^2}}\exp\left(-\frac{\mathcal{A}\rho_i^2}{2\mu_i^2}\right). \tag{20}$$

Therefore, in accordance with Eq. (17) mean values of force acting between two spots and the initial chromofield energy density are expressed as

$$< F_i >= \frac{\mu_i^2}{2}, \langle\epsilon_i\rangle = \frac{\mu_i^2}{2\mathcal{A}}. \tag{21}$$

The next step is to calculate the distribution of the total force acting between the slabs for an ensemble of events. This distribution is obtained by integrating $\delta(F - \sum_i F_i)$ over all charge densities ρ_i with weight $P(\rho_i)$. Taking for simplicity $\mu_1^2 = \ldots = \mu_n^2 = \mu^2$, we have

$$\begin{aligned} w(F) &= \prod_{i=1}^{n}\left(\int_{-\infty}^{\infty} P(\rho_i)d\rho_i\right)\delta\left(F - \frac{1}{2}\mathcal{A}\sum_{k=1}^{n}\rho_k^2\right) \\ &= \left(\frac{\mathcal{A}}{2\pi\mu^2}\right)^{n/2}\int\delta\left(F - \frac{\mathcal{A}\rho^2}{2}\right)\exp\left(-\frac{\rho^2}{\mu^2}\right) \\ &\quad\times\frac{2\pi^{n/2}}{\Gamma(n/2)}\rho^{n-1}d\rho = \frac{1}{\Gamma(n/2)\mu^2}\left(\frac{F}{\mu^2}\right)^{n/2-1}e^{-\frac{F}{\mu^2}}. \end{aligned} \tag{22}$$

In the second expression we have used $O(4)$ symmetry of the integrand and made transformation to spherical coordinates in n-dimensional ρ space. As a result we get a γ distribution which has the following first moments:

$$< F >= \frac{n}{2}\mu^2, \sigma_F = \sqrt{\frac{n}{2}}\mu^2. \tag{23}$$

One can see that the parameter μ^2 introduced in Refs. [2,6] in fact determines the mean force between the slabs and its dispersion. It is more convenient to express the mean energy density of the chromofield in the space between the slabs as

$$\epsilon_f(\tau_0) = \frac{< F >}{\sigma_0} = \frac{\mu^2}{2\mathcal{A}}. \tag{24}$$

Determination of parameter μ^2 is somewhat ambiguous. Discussion on this matter can be found in Ref. [8]. Therefore we have to use some approximation for $\epsilon_f(\tau_0)$. We will follow a simple parametrization proposed in Ref. [17],

$$\epsilon_f(\tau_0) = \epsilon_0\left(\frac{s}{s_0}\right)^{\lambda}[N_{\rm coll}(\mathbf{b}, \mathbf{s})]^{\beta}, \tag{25}$$

where ϵ_0 has a sense of the mean energy density in an individual string and is considered as an adjustable parameter. The initial time scale τ_0 corresponds to chromofield formation time which is equal to time necessary for nuclear pancakes to pass through each other. It was estimated in Ref. [29],

$$\tau_0 = \frac{1}{Q_s}e^{-\kappa/\alpha_s}, \tag{26}$$

where κ is some parameter. We assumed this time $\tau_0 \approx 0.01$ fm. This time corresponds to $\frac{\kappa}{\alpha_s} = 2.81$ at saturation momentum value $Q_s = 1.2$ GeV, calculated in Ref. [30], which corresponds to central Au + Au collisions at RHIC energies. The second factor is motivated by the small x behavior of the gluon structure function, which is consistent with $\lambda = 0.3$ [31]. The last geometrical factor is introduced to take into account the fact that, in the case of independent strings the field energy density should be proportional to the number of binary NN collisions ($\beta = 1$), but at higher energies percolated clusters of strings can be formed. As shown in Refs. [22,23], this should lead to $\beta = 0.5$. Below we assume that $\beta = 1$. Moreover, we have neglected rapidity dependence of $\epsilon_f(\tau_0)$ as follows from the transition from Eq. (13) to Eq. (15). We used different values of parameter ϵ_0 within the range $0.2 - 3.0$ GeV/fm^3. The inelastic NN cross section at RHIC energy has value $\sigma_{NN} = 4.21$ fm^2 [32]. Thus, the "charged spots" on the transverse plane, where the color charge is essentially nonzero, have the characteristic area $\mathcal{A} = \frac{\pi}{Q_s^2} \approx 0.09$ fm^2.

V. EVOLUTION OF THE CHROMOFIELD

At $t > 0$ the region occupied by the field expands following color sources at the baryonic slabs. In the other words the field is nonzero only in the region constrained by the instantaneous slab positions, $z_t(t) < z < z_p(t)$. At later time the field decays gradually into quark and gluon pairs. For our further discussion we use the light-cone variables τ, η. We incorporate approximate boost invariance of the field configurations by assuming that the field energy density is

a function of the proper time only, $\epsilon_f(\tau)$. This means that we disregard the finite size and edge effects which have been studied previously by several authors [33,34]

Let us consider several examples. In the FTM [1,3,4] the field decay is caused by the quark and gluon pair creation via the Schwinger mechanism [35]. Quite generally the evolution equation for the field energy density can be written as [4]

$$\frac{d\epsilon_f}{d\tau} = -[\kappa(2\epsilon_f)^{5/4} + 2\sigma_c\epsilon_f], \tag{27}$$

where the first term comes from the pair creation and the second one accounts for the ohmic heating of produced partons. In Ref. [3] the constant κ was estimated in the Abelian approximation for massless partons,

$$\kappa = \frac{(4\pi\alpha_s)^{5/4}\zeta(5/2)}{16\pi^3}[\nu_B + (1-2^{-3/2})\nu_F], \tag{28}$$

where $\nu_{B(F)}$ is the degeneracy factor for bosons (fermions) and α_s is the strong fine-structure constant. Corresponding degeneracy factors for quarks and gluons are

$$\nu_F = \nu_q = 2N_cN_f, \quad \nu_B = \nu_g = 2\left(N_c^2-1\right), \tag{29}$$

where $N_c = 3$ is the number of colors, and N_f is the number of quark flavors. In the numerical simulations we take $N_f = 2.5$ to take into account a nonzero mass of strange quarks. Expressions for the color conductivity σ_c can be found in Refs. [4]. At $\sigma_c = 0$ Eq. (27) has a simple analytical solution [4],

$$\epsilon_f(\tau) = \epsilon_f(\tau_0)\left[1+\frac{\tau}{\tau_d}\right]^{-4}, \tag{30}$$

where $\tau_d = 2/[\kappa(2\epsilon_0)^{1/4}]$ is a characteristic decay time and ϵ_0 is the initial field energy density. A somewhat different decay law of chromofield, $1-(\tau/\tau_d)^3$, was suggested in Ref. [5].

In the CGC model (Refs. [2,6]) the gluon field evolution is governed by nonlinear equations derived from the QCD. Without going into detail, we point out only that according to this model the chromofield has not only a transverse but also a longitudinal component. Moreover, the longitudinal fields dominate at the early times. This follows from results of Ref. [6], which were derived for the low-density limit in the covariant gauge,

$$x^+A^- + x^-A^+ = 0. \tag{31}$$

In this gauge, light-cone vector potentials of the chromofield are expressed as

$$A^\pm = \pm x^\pm\alpha(\tau, x_\perp), \tag{32}$$

where $x^\pm = (t\pm z)/\sqrt{2}$ are the light-cone coordinates and function $\alpha(\tau, x_\perp)$ is a perturbative solution of the classical Yang-Mills equation, where color charge density serves as the expansion parameter. As shown in the same paper, its Fourier transform over transverse coordinates is given by the Bessel function,

$$\alpha_k(\tau) = \alpha_k(\tau_0)\frac{2}{\omega_k\tau}J_1(\omega_k\tau), \tag{33}$$

where $\omega_k = \sqrt{\mathbf{k}_\perp^2}$, and $\mathbf{k}_\perp$ is the transverse wave vector. A longitudinal field configuration of this type was used recently in Ref. [36] as the external potential for the pair production problem in the $(1+1)$-dimensional Dirac equation. Using standard definitions, one can get the longitudinal field strength for mode $k_\perp$ as

$$\begin{aligned} E_z(\tau, \mathbf{k}_\perp) &= 2\alpha_k + \tau\frac{d\alpha_k}{d\tau} = \alpha_k(\tau_0)J_0(\omega_k\tau), \\ B_z &\approx E_z. \end{aligned} \tag{34}$$

Accordingly, the field energy density can be expressed as

$$\epsilon_f(\tau) = \tfrac{1}{2}\left(E_z^2 + B_z^2\right) = \epsilon_f(\tau_0)J_0^2(\omega_k\tau). \tag{35}$$

This solution describes damped oscillations with the characteristic period $\sim 1/\omega_k$. Asymptotically the amplitude of oscillations decreases as $1/\tau$. In our estimates below we take $\omega_k = k_\perp \approx Q_s$, where Q_s is a saturation scale (Refs. [6,30]). Since the field regeneration is physically unrealistic, we cut evolution on the first zero of the Bessel function at $\tau = 2.4/Q_s = 0.4$ fm for $Q_s = 1.2$ GeV.

Besides these two cases of field decay, we also consider an exponential decay,

$$\epsilon_f(\tau) = \epsilon_f(\tau_0)e^{-\Gamma\tau}, \tag{36}$$

which follows from Eq. (27) when the ohmic heating term is dominating. In this case $\Gamma = 2\sigma_c$, and we take $\Gamma \approx 2.5$/fm in the numerical calculations.

VI. CREATION OF PARTONIC PLASMA

Decay of the chromofield results in the production of quarks and gluons that eventually leads to the formation of thermalized quark-gluon plasma. We are not going to study here all aspects of the thermalization process. Instead, we adopt a simple picture which is often used for describing the reheating process in cosmological inflation models (see, e.g., [37]). Namely, we assume that the energy and momentum of the classical field are transferred into the equilibrated partonic plasma. In Ref. [17] this process was assumed to happen at a fixed proper time $\tau = const$. Then the energy and momentum conservation equations take a simple form,

$$T^{\mu\nu}_{\text{part}}d\Sigma_\nu = T^{\mu\nu}_{\text{field}}d\Sigma_\nu, \tag{37}$$

where the hypersurface separating the region of field and the region of plasma is parametrized as

$$d\Sigma_\mu = d^2\mathbf{s}(dz, 0, 0, -dt). \tag{38}$$

Using Eqs. (11) and (12) we can rewrite these equations explicitly as

$$[(\epsilon+p)\gamma^2 - p]dz - [(\epsilon+p)\gamma^2 v]dt = (\epsilon_f + B)dz, \tag{39}$$

$$[(\epsilon+p)\gamma^2 v]dz - [(\epsilon+p)\gamma^2 v^2 + p]dt = (\epsilon_f + B)dt, \tag{40}$$

where dz and dt are taken along the hyperbola $\tau = const$, i.e., $tdt - zdz = 0$. One can easily see that these equations require

$$v(\tau_0) = \frac{z}{t}, \epsilon(\tau_0) = \epsilon_f(\tau_0), \tag{41}$$

which are exactly the Bjorken initial conditions for scaling hydrodynamics [38].[1]

In a more realistic consideration one should deal with a continuous transformation of chromofield into plasma. Still, one can derive a simple equation for the plasma evolution even in this more general case. This is achieved by using the local energy-momentum conservation equations, $\partial_\nu T^{\mu\nu} = 0$, which give generalized hydrodynamical equations. We assume that the chromofield energy density and the plasma energy density are functions of the proper time only and are defined in the finite interval of η: $\eta_t(\tau) \leqslant \eta \leqslant \eta_p(\tau)$. As follows from Eqs. (39) and (40), in this case produced plasma has a Bjorken-like velocity field, $v = \frac{z}{t}$, and the hydrodynamical equations reduce to

$$\frac{\partial \epsilon}{\partial \tau} + \frac{\epsilon + p}{\tau} = -\frac{\partial \epsilon_f}{\partial \tau}. \tag{42}$$

This equation contains in the rhs the source term due to the parton production from the chromofield. For given $\epsilon_f(\tau)$ Eq. (42) has a simple analytical solution. Taking the equation of state for plasma in the form $p = c_s^2 \epsilon$ with constant sound velocity c_s, we get

$$\epsilon(\tau) = [\epsilon(\tau_0) + \epsilon_f(\tau_0)] \left(\frac{\tau_0}{\tau}\right)^{1+c_s^2} - \epsilon_f(\tau) + \frac{1+c_s^2}{\tau^{1+c_s^2}} \int_{\tau_0}^{\tau} \epsilon_f(\tau) \tau^{c_s^2} d\tau. \tag{43}$$

Here the initial condition for ϵ and ϵ_f is defined at proper time τ_0, which, in principle, can be moved arbitrarily close to zero. Now one can study dynamics of the plasma formation from the initial state, where the energy density was mainly stored in the chromofield.

To illustrate the general trend, let us consider an exponential field decay $\epsilon_f(\tau) = \epsilon_f(\tau_0) \exp[-\Gamma(\tau - \tau_0)]$, where the decay rate is controlled by parameter $\Gamma \approx 2.5/\text{fm}$. The integral in Eq. (43) can be done analytically for $c_s^2 = 0$. This case corresponds to free-steaming partons ($p = 0$) and is especially appropriate for the early stages of plasma evolution. Equation (43) gives in this case

$$\epsilon(\tau) = \epsilon(\tau_0)\frac{\tau_0}{\tau} + \epsilon_f(\tau_0)\left[\left(1 + \frac{1}{\tau_0\Gamma}\right)\frac{\tau_0}{\tau} - \left(1 + \frac{1}{\tau\Gamma}\right)\exp[-\Gamma(\tau - \tau_0)]\right], \tag{44}$$

where $\epsilon(\tau_0)$ is the initial energy density of partons (minijets). It is easy to find that starting from the initial state without partons $\epsilon(\tau_0) = 0$, the plasma energy density reaches its maximum value, $\epsilon_{\max} \approx 0.3\epsilon_f(\tau_0)$, at $\tau_{\max} \approx 1.79/\Gamma$. A similar behavior was found in Ref. [4] for the power-law field decay defined by Eq. (30), where $\epsilon_{\max}$ is only about $0.2\epsilon_f(\tau_0)$. In the aforementioned paper the initial field energy density was taken for the minijet initial state and evolution was started at $\tau_0 = 0.1$ fm. In our calculations we start evolution at even earlier time $\tau_0 = 0.01$ fm, corresponding to chromofield formation time (Ref. [29]), and we also neglect the minijet contribution to the energy density.

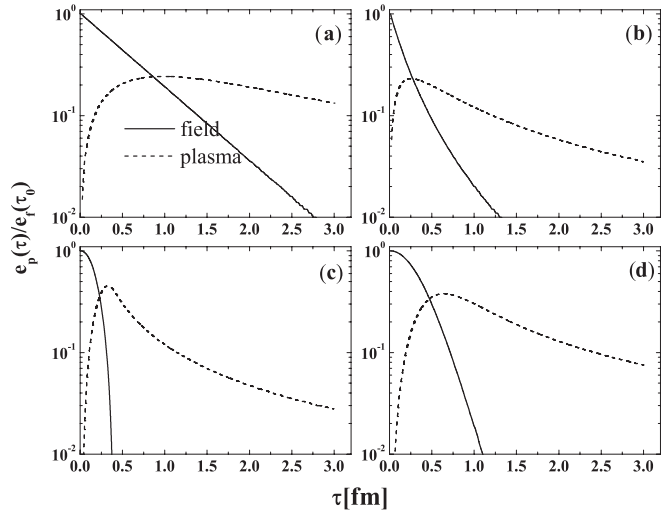

FIG. 2. Evolution of the chromofield (solid line) and QGP (dashed line) energy density in units of the initial chromofield energy densities $e_f(\tau_0)$ for different assumptions concerning chromofield decay: (a) exponential decay ($\tau_d = 0.6$ fm); (b) power-law decay ($\tau_d = 0.6$ fm); (c) CGC decay (evolution is cut at the first zero of Besel function $\tau = 2.41/Q_s$ fm, see the text); and (d) "cosh-like" chromofield decay ($\tau_d = 0.6$ fm).

A substantial reduction of the plasma energy density as compared with the initial field energy density is the common feature of all realistic calculations with the continuous plasma production. This important observation must be taken into account when estimating initial energy density of the plasma by extrapolating backward the hydrodynamical evolution.

We have considered several functional forms for the time dependence of the chromofield, resulting in the different plasma production rates and baryon deceleration patterns. Corresponding results are displayed in Fig. 2 for the exponential and power law of chromofield decay, as well as for the CGC and "cosh-like" cases. The "cosh-like" field decay given by

$$\epsilon_f(\tau) = \frac{\epsilon_f(\tau_0)}{\cosh^4[(\tau - \tau_0)/\tau_d]} \tag{45}$$

was proposed in Ref. [39] to study e^+e^- pair creation in the pulse of a strong laser field. It is seen that the maximum plasma energy density reaches only 20% of the $\epsilon_f(\tau_0)$ for the power law (30) and 40% for the CGC (35) decay law. Among all considered cases, the exponential decay law [Fig. 1(a)] leads to the longest survival of the chromofield and the slowest production of the partonic plasma.

VII. EQUATIONS OF MOTION

After the collision at $t = 0$, the trajectories of the projectile and target slabs, $z_p(t)$ and $z_t(t)$, are affected by the energy and momentum losses due to the generation of classical fields and production of partons.

[1] In Ref. [17] the terms with dt in the l.h.s. of Eqs. (39) and (40) were missing that lead to an erroneous result for $\epsilon_f(\tau_0)$ as a function of η.

First assume that the chromofields and partonic plasma are confined between the baryonic slabs. Therefore the slabs have normal vacuum from one side and excited QCD matter from the other. Then the infinitesimal decrement of the four-momentum of a slab a, dP_a^μ, after traversing distance dz in time dt, must be equal to the increment of the energy and momentum contained in the QCD bubble. The latter quantities can be expressed in terms of the energy-momentum tensor as $dP_a^\mu = T^{\mu\nu} d\Sigma_\nu$, where $d\Sigma^\nu$ is an infinitesimal four-vector orthogonal to the hypersurface constrained by dt, dz, and unit transverse area [40]. Assuming that the chromofield has only longitudinal components, the energy and momentum conservation equations can be written as

$$dE_a = -[T^{00}dz - T^{03}dt], \tag{46}$$
$$dP_a = -[T^{30}dz - T^{33}dt]. \tag{47}$$

Equations (46) and (47) describe the classical trajectories of baryonic slabs, $z_p(t)$ and $z_t(t)$, with the initial conditions $z_p(\tau_0) = z_t(\tau_0) \approx 0$, $y_p(\tau_0) = y_0$, $y_t(\tau_0) = -y_0$. Using Eqs. (10), (11), and (12), these equations can be rewritten in explicit form (for brevity we drop index a),

$$dE = -[A(\tau)\gamma^2 + B(\tau)]dz + [(A(\tau)\gamma^2 v]dt, \tag{48}$$
$$dP = -[A(\tau)\gamma^2 v]dz + [A(\tau)\gamma^2 v^2 - B(\tau)]dt, \tag{49}$$

where we have simplified the notations as

$$A(\tau) = \epsilon + p,\ B(\tau) = \epsilon_{\rm vac} + \epsilon_f - p. \tag{50}$$

It is worth noticing that $A(\tau)$ is in fact the plasma enthalpy density, and $B(\tau)$ is the total longitudinal pressure taken with negative sign. Let us rewrite the instantaneous slab velocity V and the local parton velocity v as

$$V \equiv \frac{dz}{dt} = \tanh Y,\ v = \frac{z}{t} = \tanh\eta. \tag{51}$$

Then one can derive simple kinematic relations, valid on the slab trajectories,

$$\frac{dt}{d\tau} = \frac{\cosh Y}{\cosh(Y-\eta)},\ \frac{dz}{d\tau} = \frac{\sinh Y}{\cosh(Y-\eta)},$$
$$\tau\frac{d\eta}{d\tau} = \tanh(Y-\eta). \tag{52}$$

Now we can combine Eqs. (48), (49), and (52) to the following two equations:

$$\left(\frac{dE}{d\tau}\right)^2 - \left(\frac{dP}{d\tau}\right)^2 = \left(\frac{dM}{d\tau}\right)^2 - M^2\left(\frac{dY}{d\tau}\right)^2$$
$$= [A(\tau)+B(\tau)]^2\tanh^2(Y-\eta) - B^2(\tau), \tag{53}$$

$$E\left(\frac{dE}{d\tau}\right) - P\left(\frac{dP}{d\tau}\right) = M\left(\frac{dM}{d\tau}\right)$$
$$= -A(\tau)M\sinh(Y-\eta). \tag{54}$$

After combining Eqs. (53), (54), and (52) one has

$$\frac{M}{\tau}\frac{dY}{d\eta} = A(\tau)\sinh(Y-\eta) - \frac{B(\tau)}{\sinh(Y-\eta)}. \tag{55}$$

After some additional algebra we obtain two coupled equations governing the motion of the baryonic slab:

$$\frac{d\tilde{P}}{d\tau} = -B(\tau) - \frac{\tilde{P}}{\tau}, \tag{56}$$
$$\frac{dM^2}{d\tau} = -2A(\tau)\tilde{P}, \tag{57}$$

where $\tilde{P} = M\sinh(Y-\eta)$ is the slab momentum in the local frame moving with the slab pseudorapidity η. It is interesting that the plasma enthalpy density $A(\tau)$ has dropped out from Eq. (56). In other words, the slab acceleration is determined entirely by the pressure difference $B(\tau) = \epsilon_{\rm vac} + \epsilon_f - p$ from inside and outside the QCD bubble. Obviously, the slab will decelerate only if $B(\tau) > 0$, i.e., when the field and vacuum pressure dominates over the counterpressure of the plasma. Such a situation is expected at early stages of the reaction when partonic plasma is in the free-streaming regime ($p \approx 0$). At later stages, when the field decays and plasma pressure builds up, the slab may reaccelerate again. The origin of this effect is very simple: when deriving Eqs. (56) and (57) we have implicitly assumed that the plasma particles, whose trajectories are intercepted by the slab trajectory, are absorbed by the slab. This explains also the increase of the slab mass, as predicted by Eq. (56), at $A(\tau) > 0$ and $Y < \eta$.

Equation (56) has an obvious solution,

$$\tilde{P}(\tau) = \tilde{P}_0\frac{\tau_0}{\tau} - \frac{1}{\tau}\int_{\tau_0}^{\tau} B(\tau')\tau' d\tau', \tag{58}$$

where the initial condition $\tilde{P}(\tau_0) = \tilde{P}_0$ is imposed. In the case of free motion [$B(\tau) = 0$] the first term in this equation describes gradual alignment of the initial velocity $V_0 = \tanh Y_0$ along the ray $\frac{z}{t} = V_0$ or $\lim_{\tau\to\infty}\eta(\tau) = Y_0$. From Eq. (57) one obtains the expression for the effective slab mass squared:

$$M^2(\tau) = M^2(\tau_0) - 2\int_{\tau_0}^{\tau} A(\tau')\tilde{P}(\tau')d\tau', \tag{59}$$

where $M(\tau_0) \equiv M_0$ is the initial slab mass, which was generated due to hard gluon exchange at early times, $\tau \sim 0$.

One can use the same equations to study another extreme situation, when the slabs are transparent for the partonic plasma produced at the early stages. If the plasma expands to the regions beyond the slabs, its pressure from inside and outside is equal, and one can simply drop it out from the energy-momentum conservation equations (48) and (49). It is equivalently to redefine the functions in Eq. (50) as

$$A(\tau) = 0,\ B(\tau) = \epsilon_f(\tau). \tag{60}$$

In other words the slab's motion is only affected by the residual chromofield. This case is considered below in order to understand the role of plasma back reaction (see Sec. VIII B).

Despite their simple form, Eqs. (56) and (57) reflect the important physics of ultrarelativistic nuclear collisions. Namely, they allow a study of the influence of a chromofield decay scenario and plasma back reaction on the baryon stopping. Integration of Eq. (56) was carried out by the routine based on a Chebyshev interpolation algorithm [41]. For the number of interpolation nodes $N = 40$, the 5% accuracy

was achieved as follows from the comparison with analytical results for a constant field [Eq. (64)].

VIII. SOME INTERESTING EXAMPLES

In this section we present analytical and numerical results for several physically interesting cases.

A. Vacuum cleaner

Let us first discuss a simplest case when the region between the slabs is represented by the perturbative QCD vacuum characterized by the bag constant B. This is, of course, a nonrealistic situation when no chromofield or partonic plasma is produced as the result of binary slab collisions. The baryonic slabs work in this case as a vacuum cleaner, removing all nonperturbative condensates from the region between them and forcing transition into a false vacuum state. As follows from Eq. (57) at $A(\tau) = 0$, the slab mass remains constant, $M(\tau) = M(\tau_0) = M_0$. Then the deceleration equation (58) has a very simple solution:

$$\tilde{P}(\tau) = \tilde{P}_0 \frac{\tau_0}{\tau} - \frac{B}{2\tau}\left(\tau^2 - \tau_0^2\right). \tag{61}$$

Taking $\tau_0 = 0$ we get

$$\sinh(Y - \eta) = -\left(\frac{B\tau}{2M_0}\right). \tag{62}$$

On the other hand, from Eq. (55) with $A = 0$ and $B(\tau) = B = const$ one finds that

$$\frac{dY}{\tau d\eta} = -\frac{B}{M_0 \sinh(Y - \eta)} = \frac{2}{\tau}. \tag{63}$$

With the initial condition $\eta(\tau_0) = Y_0$, this leads to the relation $\eta = (Y + Y_0)/2$. Finally we obtain the slab trajectory,

$$\eta(\tau) = Y_0 - \mathrm{Arcsinh}\left(\frac{B\tau}{2M_0}\right). \tag{64}$$

In a similar context this solution was earlier discussed in Ref. [42]. If the vacuum bubble would exist forever, Eq. (64) would predict a "yo-yo"–type motion for slab pairs [43]. In particular, the slabs will go through the turning point ($Y = 0$) at $\tau_1 = 2M_0 \sinh(Y_0/2)/B$ or $t_1 = M_0 \sinh Y_0/B$. Later on they collide again at $\eta = 0$ and $t = 2t_1$ and so on. Parametrically, the period of oscillations is long because it is proportional to $\sinh Y_0$, where Y_0 is the initial beam rapidity. In reality the vacuum bubble will decay in a much shorter time.

B. Stringy state

Now we consider multistring configurations where only the longitudinal chromo-electromagnetic fields are present. This case represents the earliest stages of the deceleration process when the fields are strong and almost no partonic plasma is present. Since in this case $A(\tau) = 0$, the slab mass remains constant, $M = M_0$, irrespective of time dependence of the field. Possible scenarios of the field evolution are described in Sec. IIC.

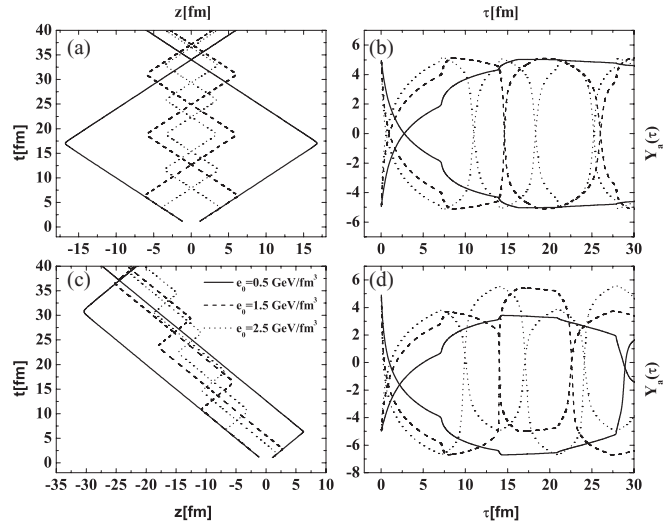

FIG. 3. Projectile and target slab trajectories on the $t - z$ plane (left panels), and projectile (upper curves) and target (lower curves) slab rapidities as functions of proper time (right panels) calculated for constant chromofield. Different pairs of curves correspond to various parameters e_0 displayed in the figure. Results are shown for two cases: (a, b) equal slabs with $N_p = N_t = 2.58$ representing a central Au + Au collision, and (c, d) $N_p = 1.01$, $N_t = 5.56$ representing peripheral collision.

Let us represent the field energy density as $\epsilon_f(\tau) = \epsilon_f(\tau_0) f(x)$, where $\epsilon_f(\tau_0)$ is its initial value parameterized in Eq. (25), and $f(x)$ is an arbitrary (decreasing) function of the dimensionless variable $x = \tau/\tau_d$, with τ_d being a characteristic decay time. Obviously, $f(x_0) = 1$, where $x_0 = \frac{\tau_0}{\tau_d}$. By introducing the dimensionless parameter

$$\alpha = \epsilon_f(\tau_0)\tau_d/M_0, \tag{65}$$

we can rewrite Eq. (58) with $\tilde{P}_0 = 0$ as

$$\sinh(Y - \eta) = -\alpha F(x),\ F(x) \equiv \frac{1}{x}\int_{x_0}^{x} f(x')x'dx'. \tag{66}$$

From Eq. (55) we get

$$\frac{dY}{d\eta} = -\alpha \frac{x f(x)}{\sinh(Y - \eta)} = \frac{x f(x)}{F(x)}. \tag{67}$$

After differentiating Eq. (66) by x and eliminating $dY/d\eta$ by Eq. (67) we get an explicit expression for the slab pseudorapidity:

$$\eta(x) = \eta(x_0) - \int_{x_0}^{x} \frac{\alpha F(x')}{\sqrt{(\alpha F(x'))^2 + 1}} \frac{dx'}{x'}. \tag{68}$$

Now calculations can be easily done for any specific $f(x)$. For instance, the choice $f(x) = 1$ corresponds to the time-independent chromofield, $\epsilon_f(\tau) = \epsilon_f(\tau_0)$, which is formally equivalent to the false vacuum case considered in the previous section. In this case $F(x) = x/2$ (for $x_0 = 0$) and, apart from notations, Eq. (68) gives the same result as Eq. (64). Numerical calculations of slab rapidities $Y_a(\tau)$ and slab trajectories $z_a(\tau)$ corresponding to this case are displayed in Fig. 3. At each intersection of slab trajectories, the constant chromofield changes sign and initial conditions are recalculated. Each

instant of collision of two slabs corresponds to their maximum rapidities. This can be easily seen in the behavior of trajectories and rapidities of two identical slabs [Figs. 3(a) and 3(b)]. In this case laboratory time coincides with the proper time, $t_1 = \tau_1$. In asymmetric collisions [Figs. 3(c) and 3(d)] energy loss of the smaller projectile slab is larger than energy loss of the target slab. After the second collision the projectile slab reaccelerates and gains kinetic energy larger than the initial one. Deceleration and reacceleration of the target slab is smaller due to its larger mass. This periodic motion states a challenge for the numerical simulations. Sufficient accuracy to find initial conditions at each intersection point was achieved only by increasing the number of nodes in Chebyshev interpolation from 40 to 60. It is seen that the constant chromofield leads to the yo-yo–type motion of baryonic slabs, with the period strongly dependent on the initial slab rapidity and the chromofield energy density. This is in direct analogy with the Lund model for e^+e^- annihilation [44] and other string-based models. The principle difference in our approach is that we describe the coherent action of many stringlike configurations (17).

Let us consider now several more realistic time-dependent fields as discussed in Sec. V:

(1) The field evolution motivated by the Schwinger mechanism [Eq. (30)] is described by $f(x) = (1+x)^{-4}$, which gives

$$F(x) = \frac{1}{x}\int_0^x \frac{x'dx'}{(1+x')^4} = \frac{x(3+x)}{6(1+x)^3}. \qquad (69)$$

(2) The exponential decay, $f(x) = e^{-\gamma x}$ with $\gamma = \Gamma\tau_d = 1$, corresponds to

$$F(x) = \frac{1}{x}\int_0^x e^{-x'}x'dx' = \frac{1}{x}(1-e^{-x}). \qquad (70)$$

(3) The CGC-motivated decay, which leads to sharp disappearance of the field at $\tau_d \approx 2.4/Q_s$, i.e., to $F(x) = const$ at $x > 1$.

In Figs. 4–6 we show the slab trajectories $z_a(\tau)$ as a function of proper time. It is instructive to compare them with trajectories calculated for the constant field (Fig. 3). Due to the fast decay of the chromofield we generally do not observe any traces of the yo-yo motion. Peripheral collisions with large $\epsilon_f(\tau_0)$ and without taking into account plasma back reaction gives the largest deceleration of the projectile slab [Fig. 7(d)]. The increasing of impact parameter and ϵ_0 will eventually lead to reversal of the slab trajectories and their further collisions. The back reaction of the plasma generates a strong push to the slabs. For comparison, the distance between colliding slabs with equal baryon number ($N_p = N_t = 5.74$) corresponding to the proper time $\tau = 1.91$ fm for the case with plasma back reaction, is $\Delta z = 64.54$ fm, and for the case when plasma back reaction was not taken into account, is $\Delta z = 25.35$ fm, if $\epsilon_f(\tau_0)$ parameter $\epsilon_0 = 1$ GeV/fm^3 was chosen, and the power of chromofield decay was considered. Numerical results for evolution of the collective slab rapidities are presented in Figs. 7–9. Calculations were performed for the values of parameter ϵ_0 ranging from 0.2 to 1.0 GeV/fm^3 and two values of impact parameter. By comparing left and rights panels,

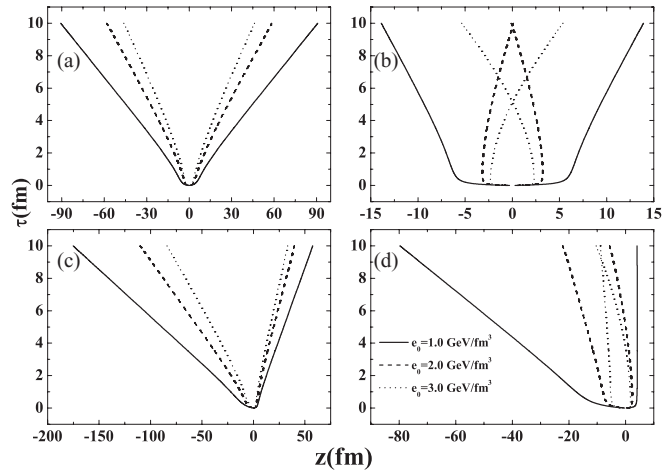

FIG. 4. Projectile (right curves) and target (left curves) slab trajectories on $z-\tau$ plane calculated for the exponential chromofield decay with $\tau_d = 0.4$ fm. Different pairs of curves correspond to the different parameters ϵ_0 displayed in the figure. Results are shown for two cases: (a, b) equal slabs with $N_p = N_t = 5.8$ representing a central Au + Au collision, and (c, d) $N_p = 2.0$, $N_t = 8.8$ representing a central d + Au collision. Left and right panels show the calculations with and without the back reaction of produced plasma, respectively.

one can see in this figures that the slab dynamics is strongly affected by the plasma back reaction. Namely, the plasma back reaction leads to rapid saturation of the baryon rapidity loss with increasing $\epsilon_f(\tau_0)$. It is seen also that the rapidity lost by the smaller slab is significantly larger than the bigger one. This is, of course, a direct consequence of Newton's law that the equal forces cause larger deceleration for less massive bodies. This result is in agreement with STAR measurements for net-baryon spectra reconstructed from net-Λ production spectra in d + Au collisions, Ref. [45].

In Fig. 10 projectile rapidity loss is displayed as a function of beam rapidity calculated in the wide interval from RHIC to Large Hadron Collider (LHC) energies at the different parameters ϵ_0. It is seen that strong counterpressure of plasma

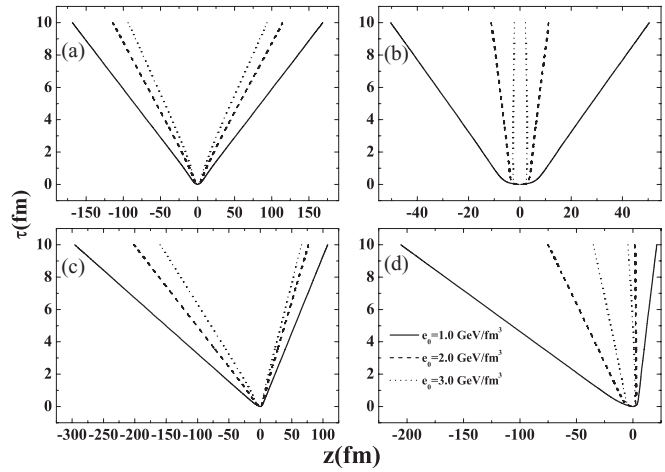

FIG. 5. The same as Fig. 4 but for the power-law chromofield decay.

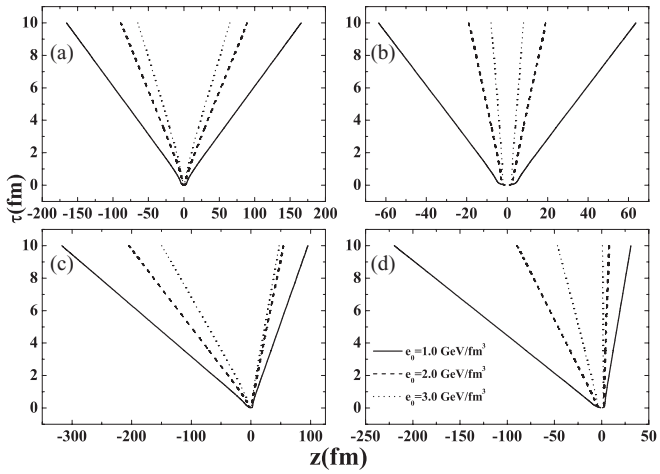

FIG. 6. The same as Fig. 4 but for the CGC decay law of chromofield decay Eq. (35), with $Q_s = 1.2$ GeV.

on slabs leads to slight violation from the linear growth of baryon energy loss with increasing the ϵ_0.

In Fig. 11 we show the evolution of the projectile slab energy loss $\Delta E_p(\tau)$ per baryon, defined as

$$\Delta E_p(\tau) = [M_0 \cosh Y_0 - M_p(\tau) \cosh Y_p(\tau)]/N_p, \quad (71)$$

where M_0 is the initial slab mass and $M_p(\tau)$ is the projectile slab mass calculated by formula (59), and N_p is the baryon number of projectile slab. The additional slab transverse mass $M_p(\tau)$ is generated entirely due to interaction with produced plasma. To demonstrate the strength of this interaction, in

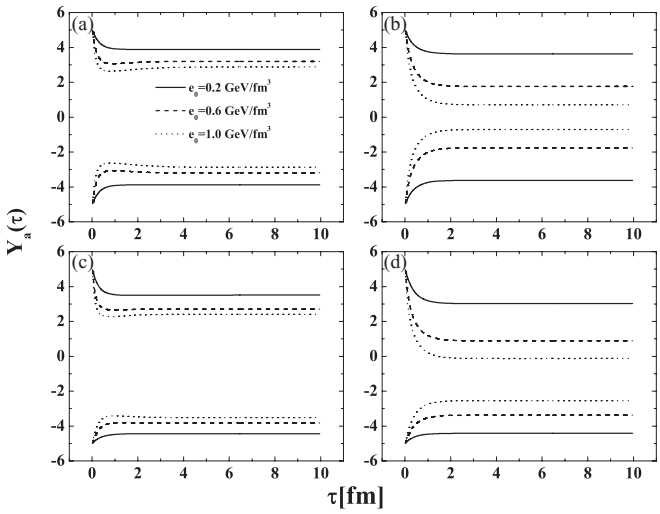

FIG. 7. Projectile (upper curves) and target (lower curves) slab rapidities as functions of proper time calculated for the exponential law of chromofield decay with $\tau_d = 0.6$ fm. Different pairs of curves correspond to different parameters ϵ_0 displayed in the figure. Results are shown for two cases: (a, b) equal slabs with $N_p = N_t = 5.8$ representing a central Au + Au collision, and (c, d) $N_p = 2.0$, $N_t = 8.8$ representing a central d + Au collision. Left and right panels show the calculations with and without the back reaction of produced plasma, respectively.

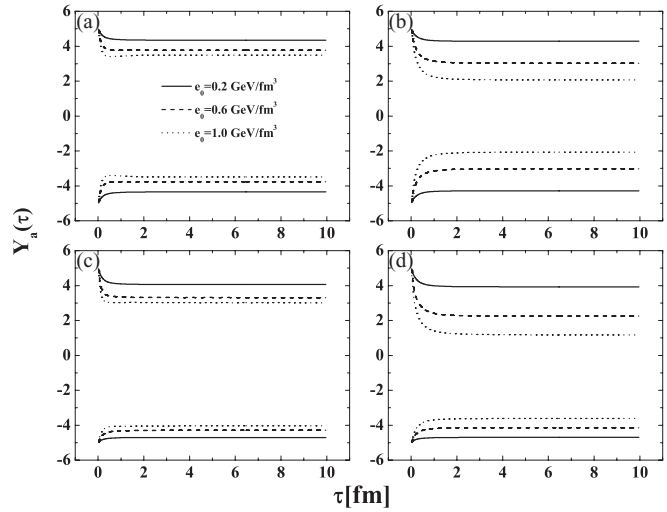

FIG. 8. The same as Fig. 7 but for the power law of chromofield decay with $\tau_d = 0.6$ fm.

Fig. 12 we show the evolution of the baryon transverse momentum. The maximal value of baryon transverse momentum for central collisions is quite large: $\langle p_\perp \rangle = 3.5$ GeV if we take as initial value $\langle p_\perp \rangle \approx 1$ GeV, which was extracted from experimental data [10]. To obtain such a low value of baryon transverse momentum one has to take into account partial transparency of slabs with respect to the produced plasma. This can be implemented by assuming that plasma is created not uniformly on the whole hypersurface $\tau = const$, but only on the part of it which is sufficiently far from the ends (edge effect). Thus, in a more realistic calculation, dependence of the plasma energy density on pseudorapidity should be explicitly taken into account. When the plasma back reaction is disregarded, the slab mass remains constant in the course of evolution. Therefore, we should assume that the observed value of the baryon transverse momentum was generated already at the very early stage of the collisions, i.e.,

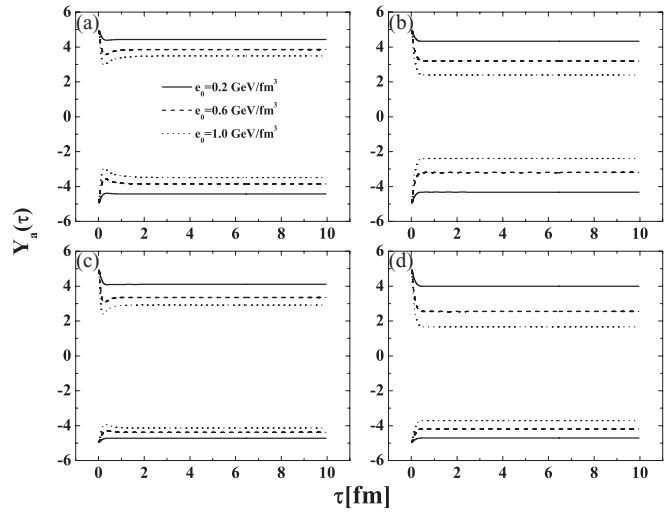

FIG. 9. The same as Fig. 7 but for the CGC decay law of chromofield decay [Eq. (35)], with $\tau_d = 0.4$ fm.

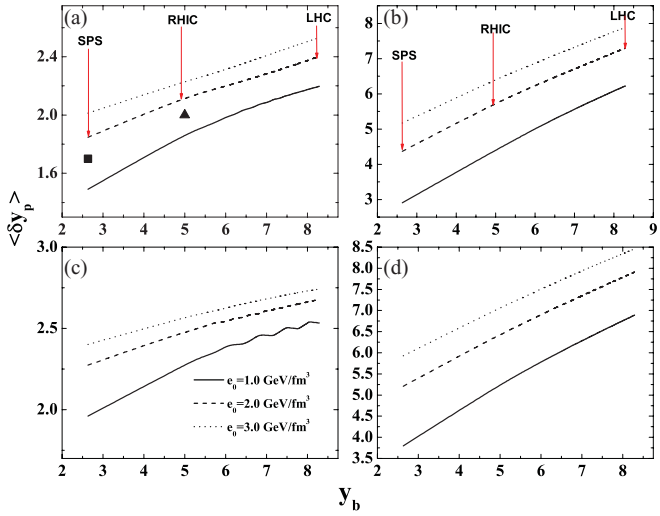

FIG. 10. (Color online) Projectile slab rapidity loss as a function of initial beam rapidity calculated for the power law of chromofield decay. Different curves correspond to the different values of parameter ϵ_0 displayed in the figures. Color charge is assumed fixed. Results are shown for the two cases: (a, b) equal slabs with $N_p = N_t = 5.75$ representing a central Au + Au collision, and (c, d) $N_p = 2.01$, $N_t = 7.65$ representing central d + Au collision. Left and right panels show the calculations with and without the back reaction of produced plasma, respectively. The filled square corresponds to SPS data, and the filled triangle to RHIC data

at $\tau \sim \tau_0$. Then the initial slab rapidities should also be shifted from y_0 to $y_0 = \text{Arccosh}(\frac{\sqrt{s}}{2m_\perp})$. From Fig. 11 one can see that the 70% energy loss observed by the BRAHMS collaboration for central Au + Au collisions at $\sqrt{s} = 200$ AGeV can be

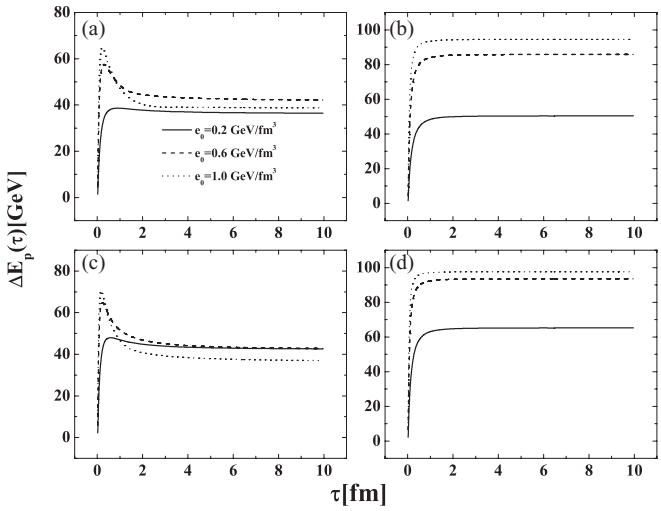

FIG. 11. Evolution of the baryon energy loss from the projectile nucleus calculated for power-law chromofield decay with $\tau_d = 0.6$ fm. Different curves correspond to the different values of parameter ϵ_0 displayed in the figures. Results are shown for the two cases: (a, b) equal slabs with $N_p = N_t = 5.75$ representing a central Au + Au collision, and (c, d) $N_p = 2.01$, $N_t = 7.65$ representing central d + Au collision. Left and right panels show the calculations with and without the back reaction of produced plasma, respectively.

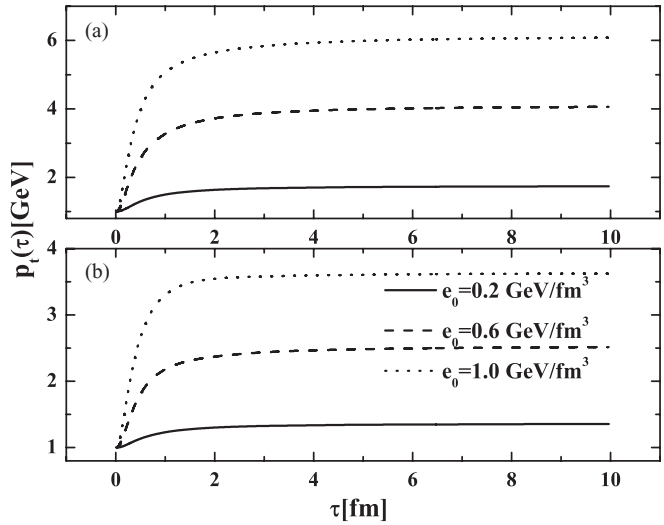

FIG. 12. Evolution of the baryon transverse momentum calculated for the power law of chromofield decay at different parameters ϵ_0 indicated in the figure. Results are shown for two cases: (a) $N_p = N_t = 5.75$ representing central Au + Au collisions, and (b) $N_p = 2.01$, $N_t = 7.65$ representing central d + Au collisions.

explained by the action of the chromofield with the energy density of about 20 GeV/fm^3 ($\epsilon_0 \simeq 0.5$ GeV/fm^3).

C. Partonic wind

In this subsection we address the question of how the baryon slab trajectories are affected by the collective partonic flux from the central region. The calculations can be done analytically for a steplike evolution of the chromofield, $\epsilon_f(\tau) = \epsilon_f(\tau_0)\theta(\tau_d - \tau)$. In this case the partonic plasma is produced at a fixed proper time $\tau = \tau_d$, exactly as postulated in the Bjorken model [38]. An interesting observation for this case is that predictions can be made without knowledge of equation of state. According to Eqs. (43) and (50), the pressure, energy density, and enthalpy density of partonic plasma at later times ($\tau > \tau_d$) evolve as

$$p(\tau) = c_s^2\epsilon(\tau) = c_s^2\epsilon_f(\tau_0)\left(\frac{\tau_d}{\tau}\right)^{1+c_s^2},$$
$$A(\tau) = \left(1+c_s^2\right)\epsilon_f(\tau_0)\left(\frac{\tau_d}{\tau}\right)^{1+c_s^2}, \quad (72)$$

where c_s^2 is the constant sound velocity. From Eq. (58) we find that due to the action of the chromofield at $\tau < \tau_d$, the slab momentum decreases on the value $\tilde{P}(\tau_d) - \tilde{P}(0) = -\epsilon_f(\tau_0)\tau_d/2$. The additional momentum change due to the partonic wind at $\tau > \tau_d$ is found from Eq. (58) with $B(\tau) = -p(\tau)$:

$$\tilde{P}(\tau) - \tilde{P}(\tau_d) = -\frac{\epsilon_0\tau_d^2}{2\tau} - \epsilon_0\tau_d\left(\frac{c_s^2}{1-c_s^2}\right)\left[\left(\frac{\tau_d}{\tau}\right)^{c_s^2} - \left(\frac{\tau_d}{\tau}\right)\right]. \quad (73)$$

According to Eq. (59) with $A(\tau)$ from Eq. (72), the additional slab mass squared due to plasma absorption is given

by

$$M^2(\tau) - M^2(\tau_0) = -\frac{\epsilon_0^2 \tau_d^2}{1 - c_s^2}\left(\frac{1 - 3c_s^2}{x^{1+c_s^2}} + \frac{1 + c_s^2}{x^{2c_s^2}} + 2\left(c_s^2 - 1\right)\right)\Bigg|_1^{\tau/\tau_d}, \quad (74)$$

where $x = \frac{\tau}{\tau_d}$ is a new variable. Asymptotically at $\tau \to \infty$ dependence on the sound velocity in the relative mass squared increment drops out:

$$\frac{M^2 - M_0^2}{M_0^2} = 2\alpha^2. \quad (75)$$

Parameter α was introduced in Eq. (65). Let us take $\epsilon_0 = 1.0$ GeV/fm^3, which according to Eq. (25) corresponds to average energy density for central Au + Au collisions $\epsilon_f(\tau_0) = 30.65$ GeV/fm^3. The initial mass per unit area of the central slab is $M(\tau_0) = 2.89$ GeV/fm^2. The characteristic time of chromofield decay was chosen as $\tau_d = 0.6$ fm. For these values parameter α is estimated as $\alpha = 6$. This eventually leads to an increase of the slab mass by ~8.5 times, which is obviously unrealistic.

IX. SUMMARY

A new model was proposed where net-baryon stopping and associated particle production are attributed to strong chromofields generated at early stages of a heavy-ion collision.

In this model the Lorentz contracted nuclei (nuclear sheets) are divided into small slabs which are pairwise connected by the color flux tubes. The QGP is produced as a result of the chromofield decay. Equations describing slab trajectories as well as time evolution of their masses and rapidities are derived from explicit energy-momentum conservation across the slab. The creation and evolution of the plasma was described by a simple hydrodynamical equation with a simple source term corresponding to chromofield decay. The stochastic nature of color charges based on the CGC model was also taken into account. Different scenarios of chromofield decay were studied numerically. It was shown that due to the delayed QGP production its maximum energy density reaches only 20%–40% of the initial chromofield energy density. Baryon-rich as well as baryon-free components of the QGP are treated as ideal fluids. Interaction between these fluids leads to increasing slab temperature and, therefore, to increasing transverse momentum of produced baryons.

In the case of the power law of chromofield decay, the observed net-baryon rapidity loss in central Au + Au collisions at RHIC energy $\sqrt{s} = 200$ A GeV, $\langle \delta y \rangle \approx 2$, can be reproduced if the initial energy density is $\epsilon_f(\tau_0) = 99.55$ GeV/fm^3 in the variant of calculations, which takes into account plasma back reaction ($\langle \delta y \rangle = 1.94$), and a smaller value of initial chromofield energy density $\epsilon_f(\tau_0) = 19.91$ GeV/fm^3 should be taken if there is no plasma back reaction ($\langle \delta y \rangle = 2.01$) (see also Fig. 10). Extrapolation to the LHC energy $\sqrt{s} = 5500$ A GeV leads to $\langle \delta y \rangle = 2.31$ in the case with plasma back reaction and $\langle \delta y \rangle = 3.92$ in the case without plasma back reaction, with initial chromofield energy densities $\epsilon_f(\tau_0) = 265.05$ GeV/fm^3 and $\epsilon_f(\tau_0) = 53.81$ GeV/fm^3, correspondingly.

ACKNOWLEDGMENTS

The authors thank C. Greiner, M. Gyulassy, L. McLerran, L. M. Satarov, and H. Stöcker for useful discussions. This work was supported in part by the DFG, Grant No. 436RUS 113/711/0-2 (Germany), and Grant Nos. RFFR-05-02-04013 and NS-8756.2006.2 (Russia). One of the authors (K.L.) acknowledges J.W. Göthe Univeristät for generous financial support and the CSC cluster for computational time. This work was partly supported by the Priority Research Centers Program through the National Research Foundation of Korea (NRF), funded by the Ministry of Education, Science and Technology (2010-0020077). H.J.L. and K.L. were supported by a grant from "the 2nd phase BK21 project."

[1] A. Casher, H. Neuberger, and S. Nussinov, Phys. Rev. D **20**, 179 (1979); N. K. Glendenning and T. Matsui, Nucl. Phys. B **245**, 449 (1984) ; K. Kajantie and T. Matsui, Phys. Lett. B **164**, 373 (1985); M. Gyulassy and A. Iwazaki, *ibid.* **165**, 157 (1985).
[2] L. McLerran and R. Venugopalan, Phys. Rev. D **49**, 2233 (1994); **49**, 3352 (1994); **50**, 2225 (1994); **59**, 094002 (1999); arXiv:hep-ph/0202270.
[3] G. Gatoff, A. K. Kerman, and T. Matsui, Phys. Rev. D **36**, 114 (1987).
[4] K. J. Eskola and M. Gyulassy, Phys. Rev. C **47**, 2329 (1993).
[5] L. Wilets and R. D. Puff, Phys. Rev. C **51**, 339 (1995).
[6] A. Kovner, L. McLerran, and H. Weigert, Phys. Rev. D **52**, 3809 (1995); **52**, 6231 (1995).
[7] S. Jeon and R. Venugopalan, Phys. Rev. D **70**, 105012-1 (2004).
[8] M. Gyulassy and L. McLerran, Phys. Rev. C **56**, 2219 (1997).
[9] G. Gatoff, A. K. Kerman, and D. Vautherin, Phys. Rev. D **38**, 96 (1988).
[10] I. G. Bearden *et al.* (BRAHMS Collaboration), Phys. Rev. Lett. **94**, 032301 (2005).
[11] S. A. Bass *et al.*, Prog. Part. Nucl. Phys. **41**, 225 (1998).
[12] N. S. Amelin, N. Armesto, C. Pajares, and D. Souza, Eur. Phys. J. C **22**, 149 (2001).
[13] K. Itakura, Yu. Kovchegov, L. McLerran, and D. Teaney, Nucl. Phys. A **730**, 160 (2004).
[14] S. A. Bass, B. Muller, and D. K. Srivastava, Phys. Rev. Lett. **91**, 052302 (2003).
[15] M. Hirai, S. Kumano, and K. Saito, arXiv:1102.3479v2 [hep-ph].
[16] [http://research.kek.jp/people/kumanos/nuclp.html].
[17] I. N. Mishustin and J. I. Kapusta, Phys. Rev. Lett. **88**, 112501 (2002).
[18] I. N. Mishustin and K. A. Lyakhov, Phys. Rev. C **76**, 011603(R) (2007).
[19] Yu. B. Ivanov, I. N. Mishustin, and L. M. Satarov, Nucl. Phys. A **433**, 713 (1985).

[20] R. J. Glauber, in *Lectures on Theoretical Physics*, edited by W. E. Brittman and L. G. Dunham (Interscience, New York, 1959), Vol. 1, p. 315.
[21] T. Lappi and L. McLerran, Nucl. Phys. A **772**, 200 (2006).
[22] S. Fortunato, F. Karsch, P. Petreczky, and H. Satz, Phys. Lett. B **502**, 321 (2001).
[23] M. A. Braun, F. del Moral, and C. Pajares, Phys. Rev. C **65**, 024907 (2002).
[24] L. D. Landau and I. M. Lifshits, *The Field Theory* (Plenum, New York, 1964).
[25] H. B. Nielsen and P. Olesen, Nucl. Phys. B **61**, 45 (1973).
[26] G. Martens, C. Greiner, S. Leupold, and U. Mosel, Phys. Rev. D **70**, 116010 (2004).
[27] P. Goddard, J. Goldstone, C. Rebbi, and C. B. Thorn, Nucl. Phys. B **56**, 109 (1973).
[28] L. V. Gribov, E. M. Levin, and M. G. Ryskin, Phys. Rep. **100**, 1 (1983); D. Kharzeev, E. Levin, and K. Tuchin, Phys. Rev. C **75**, 044903 (2007).
[29] L. McLerran, Int. J. Mod. Phys. A **25**, 5847 (2010); arXiv:0812.1506 [hep-ph].
[30] D. Kharzeev and M. Nardi, Phys. Lett. B **507**, 121 (2001).
[31] L. McLerran, arXiv:hep-ph/0402137.
[32] D. Kharzeev, C. Lourenco, M. Nardi, and H. Satz, Z. Phys. C **74**, 307 (1997).
[33] R. C. Wang and C. Y. Wong, Phys. Rev. D **38**, 348 (1988).
[34] C. Martin and D. Vautherin, Phys. Rev. D **38**, 3593 (1988).
[35] J. Schwinger, Phys. Rev. **82**, 664 (1951); (see also F. Sauter, Z. Phys. **69**, 742 (1931); W. Heisenberg and H. Euler, *ibid*. **98**, 714 (1936)).
[36] F. Gelis, K. Kajantie, and T. Lappi, Phys. Rev. C **71**, 024904 (2005).
[37] E. Kolb and M. Turner, *The Early Universe* (Addison-Wesley, Redwood City, CA, 1990).
[38] J. D. Bjorken, Phys. Rev. D **27**, 140 (1983).
[39] A. A. Grib, S. G. Mamaev, and V. M. Mostepanenko, *Vacuum Quantum Effects in Strong External Fields* (Atomizdat, Moscow, 1988).
[40] F. Cooper and G. Frye, Phys. Rev. D **10**, 186 (1974).
[41] W. H. Press *et al*., *Numerical Receipes on Fortran* (Cambridge University Press, 1988), p. 151.
[42] A. Bialas, W. Czyz, A. Dyrek, and W. Florkowski, Z. Phys. C **46**, 439 (1990).
[43] A. Bialas and W. Czyz, Phys. Rev. D **31**, 198 (1985).
[44] B. Andersson, G. Gustafson, and G. Ingelman, Phys. Rep. **97**, 31 (1983).
[45] B. I. Abelev *et al*., Phys. Rev. C **76**, 64904 (2007).